Tunable double Weyl phonons driven by chiral point group symmetry

Y. J. Jin,[1,2] Z. J. Chen,[1,3] X. L. Xiao,[1,4] and H. Xu[1,5,*]

[1]*Department of Physics & Institute for Quantum Science and Engineering, Southern University of Science and Technology, Shenzhen 518055, People's Republic of China*

[2]*Department of Physics, the University of Hong Kong, Pokfulam Road, Hong Kong, People's Republic of China*

[3]*Department of Physics, South China University of Technology, Guangzhou 510640, People's Republic of China*

[4]*Institute for Structure and Function & Department of physics, Chongqing University, Chongqing 400044, People's Republic of China*

[5]*Guangdong Provincial Key Laboratory of Computational Science and Material Design & Shenzhen Key Laboratory for Advanced Quantum Functional Materials and Devices, Southern University of Science and Technology, Shenzhen 518055, People's Republic of China*

(Received 22 June 2020; accepted 22 February 2021; published 5 March 2021)

Different from spin-$\frac{1}{2}$ Weyl points which are robust due to the protection of topology, the unconventional chiral quasiparticles usually require extra crystalline symmetries for their existence, indicating that such quasiparticles are sensitive to perturbation. Herein, we present that the spin-1 Weyl can transform into quadratic Weyl phonons depending on symmetry variation. Specifically, the spin-1 Weyl nodes arisen from three-dimensional (3D) irreducible representations (IRs) of chiral point groups, $O(432)$ or $T(23)$, are verified to split into quadratic Weyl points if symmetry breaking decomposes 3D IRs into two-dimensional IRs. Symmetry analysis and low-energy effective models are performed to identify the splitting mechanisms. The evolution of Berry curvature and surface states driven by symmetry breaking is obtained in real materials. Our work not only builds the connection between double Weyl phonons but also offers guidance for exploring the transition among unconventional quasiparticles.

DOI: 10.1103/PhysRevB.103.104101

I. INTRODUCTION

Band topology has sparked intense studies in the last few years [1–16]. The interplay between symmetry and topology has provided a useful way to find new topological states and helps us to understand the possible topological phases in solid-state physics [1–3]. In this light, various symmetry protected topological nontrivial states are discovered, i.e., topological insulators [4,5], Dirac semimetals [6–9], Weyl semimetals [10–12,16–18], and node-line semimetals [13–15,19,20], etc. Among them, the chiral fermions characterized by topological charge (Chern number $\mathcal{C}$) receive much attention because of their chiral anomaly [21–24].

Different from the free fermions constrained by the Poincaré symmetry, the low-energy fermionic excitations in condensed-matter physics need to respect the space group symmetry in three-dimensional (3D) lattices [25]. As a result, unconventional chiral quasiparticles without counterparts in high-energy physics are proposed. They range from two-, three-, four-, and sixfold degeneracies characterized by Chern number $\mathcal{C}$ larger than one [25–31]. Among them, the chiral quasiparticles which carry Chern number $\mathcal{C}$ of ± 2 are called double Weyl nodes and come in three types [30]. The first type is the threefold spin-1 Weyl point [26], which is protected by spatial symmetry and can be described by a low-energy $\boldsymbol{k}\cdot\boldsymbol{p}$ Hamiltonian $\boldsymbol{H} = \mathbf{k}\cdot\mathbf{S}$, where $\mathbf{S}$ is a 3×3 matrix taken as the generating operators of SO(3) rotation group in the spin-1 representation [25]. For spin-1 Weyl point, the three bands carry Chern numbers $\mathcal{C}$ of ± 2, 0 (see the left panel of Fig. 1). The second type is the twofold degenerate node, in which the linear terms are suppressed by spatial or time reversal $\mathcal{T}$ symmetries [27,29] (see the blue lines in right panel of Fig. 1). Moreover, a quadratic Weyl node and two spin-$\frac{1}{2}$ Weyl points with opposite chirality can form a triangular Weyl complex [32,33]. In the third type, the double Weyl nodes are formed by fourfold band crossings, which can be considered as the direct sum of two Weyl equations with the same chirality related by $\mathcal{T}$ symmetry. Each spin-$\frac{1}{2}$ Weyl point contributes a unit topological charge, giving birth to the fourfold double Weyl fermions with $\mathcal{C} = \pm 2$ [30].

Incorporating symmetries with topology has enriched the topological classification and promises new varieties of phenomena different from the conventional ones. For example, the intriguing electronic and optical transport phenomena stem from large Chern number $\mathcal{C}$ [34,35], quantum criticality, and phase transition [36,37], etc. However, symmetry protected unconventional quasiparticles become susceptible to perturbation. Up to now, the splitting mechanisms of unconventional quasiparticles in boson systems are still lacking. It is rational to explore their splitting behaviors under symmetry breaking.

In this work, to uncover the splitting mechanisms of unconventional quasiparticles, we simply focus on the spin-1 Weyl phonons emerging at the center of the Brillouin zone (BZ). We show that the space groups whose isogonal point groups are either $O(432)$ or $T(23)$ groups can host spin-1 Weyl points at Γ due to the existence of 3D irreducible

*xuh@sustech.edu.cn

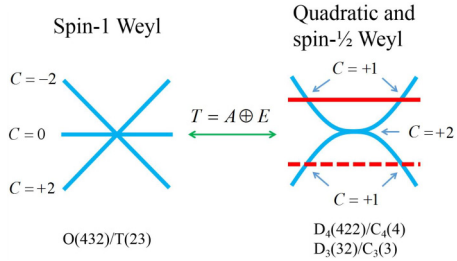

FIG. 1. The transition between the spin-1 Weyl (left panel) and quadratic (right panel) Weyl nodes driven by $T = A \oplus E$. In the left panel, the spin-1 Weyl nodes are managed by 3D IRs of $O(432)$ or $T(23)$. The three bands are labeled by Chern numbers $\mathcal{C}$ with the values of ± 2, 0, respectively. In the right panel, the quadratic Weyl points ($\mathcal{C} = +2$) are guaranteed by 2D IRs of the subgroups, i.e., $D_4(422)$, $C_4(4)$, etc. The third single band is accidentally either above (red solid line) or below (red dashed line) the quadratic Weyl point to form spin-$\frac{1}{2}$ Weyl nodes ($\mathcal{C} = +1$).

representations (IRs). Furthermore, the spin-1 Weyl points will split into quadratic Weyl nodes if the 3D IRs decompose into two-dimensional (2D) IRs, $T = A \oplus E$, where T, E, and A represent the triple, double, and single IRs, respectively. All possible degenerations following $T = A \oplus E$ are tabulated in Table I. According to the criteria, the involved space groups possessing either spin-1 or quadratic Weyl points at Γ are given in Table S1 in the Supplemental Material (SM) [38]. If crystalline symmetries are further broken, the quadratic Weyl points will split into one pair of spin-$\frac{1}{2}$ Weyl nodes with the same chirality. Low-energy effective $\boldsymbol{k} \cdot \boldsymbol{p}$ models and symmetry arguments are performed to verify the transition behaviors of the double Weyl nodes. Furthermore, based on first-principles calculations, $Rb_2Be_2O_3$ and $SrSi_2$ are provided to support our analysis.

II. LOW-ENERGY EFFECTIVE MODELS

In a low-energy effective model, the symmetries require the Hamiltonian $H(\mathbf{k})$ satisfying the equation,

$$D_m H(\mathbf{k}) D_m^{-1} = H(R_m \mathbf{k}), \tag{1}$$

where D_m is the generating operator, and R_m is the corresponding matrix representation.

We first consider a generic 3D lattice with a point group $O(432)$. The generating elements are chosen as twofold rotational symmetry $\mathcal{C}_{2x}$ along the [100] axis, threefold rotational symmetry $\mathcal{C}_{3[111]}$ along the [111] direction, fourfold rotational symmetry $\mathcal{C}_{4z}$ along the [001] axis, and the time reversal symmetry $\mathcal{T}$. Here, all the rotational operators are uniformly anticlockwise ones. The corresponding 3D matrix representations [39] can be written as

$$\mathcal{C}_{2x} = \begin{pmatrix} -1 & 0 & 0 \\ 0 & 1 & 0 \\ 0 & 0 & -1 \end{pmatrix}, \quad \mathcal{C}_{3[111]} = \begin{pmatrix} 0 & 0 & 1 \\ 1 & 0 & 0 \\ 0 & 1 & 0 \end{pmatrix}, \quad \mathcal{C}_{4z} = \begin{pmatrix} -1 & 0 & 0 \\ 0 & 0 & 1 \\ 0 & -1 & 0 \end{pmatrix}, \quad \mathcal{T} = \mathcal{K}, \tag{2}$$

where $\mathcal{K}$ is a complex conjugation operator. The transformation of momentum $\mathbf{k}$ under generating operators is listed below,

$$\begin{aligned} (k_x, k_y, k_z) &\xrightarrow{\mathcal{C}_{2x}} (k_x, -k_y, -k_z), \\ (k_x, k_y, k_z) &\xrightarrow{\mathcal{C}_{3[111]}} (k_z, k_x, k_y), \\ (k_x, k_y, k_z) &\xrightarrow{\mathcal{C}_{4z}} (-k_y, k_x, k_z), \\ (k_x, k_y, k_z) &\xrightarrow{\mathcal{T}} (-k_x, -k_x, -k_z). \end{aligned} \tag{3}$$

We then have the low-energy effective model H_o with the linear orders to respect Eq. (1),

$$H_o = m \begin{pmatrix} 0 & -ik_y & ik_x \\ ik_y & 0 & -ik_z \\ -ik_x & ik_z & 0 \end{pmatrix}, \tag{4}$$

where the coefficient m is a nonzero real constant. Here, the constant m is set to 1 to calculate the dispersion relation [see Fig. S1(a)]. The Chern number $\mathcal{C}$ is obtained by the Wilson loop method [40]; see Fig. S1(d). We find each band has a Chern number $\mathcal{C}$ of ± 2, 0, respectively, indicating the expected spin-1 Weyl point.

We next examine the splitting behaviors of spin-1 Weyl points by introducing a perturbation Hamiltonian with $\mathcal{C}_3$ symmetry breaking. After removing $\mathcal{C}_{3[111]}$ from the generating operators, the remaining operators $\mathcal{C}_{2x}$, $\mathcal{C}_{4z}$, and $\mathcal{T}$ symmetries in Eq. (2), are automatically the subduced representations under $\mathcal{C}_3$ symmetry breaking. Therefore, the constructed perturbation Hamiltonian V shares the same basis functions with the H_o and can be described by

$$V = \begin{pmatrix} m_1 & -g_1 ik_y & g_1 ik_x \\ g_1 ik_y & 0 & g_2 ik_z \\ -g_1 ik_x & -g_2 ik_z & 0 \end{pmatrix}, \tag{5}$$

where the coefficients m_1, g_1, and g_2 are nonzero real constants. The final Hamiltonian H can be written as

$$H = H_o + V. \tag{6}$$

The quadratic Weyl points derived from spin-1 Weyl nodes by breaking $\mathcal{C}_3$ symmetry can be described by Eq. (6). After introducing the perturbation, the little group at Γ decreases into $D_4(422)$, and 3D IRs associated with $O(432)$ simultaneously decompose into 2D IRs. To examine the topology of the Hamiltonian H in Eq. (6), the parameters are chosen as

TABLE I. Compatibility table for $O(432)$ group.

O	T	D_4	D_3	C_4	C_3
A_1	A	A_1	A_1	A	A
A_2	A	B_1	A_2	B	A
E	$\{^1E,^2E\}^*$	$A_1 + B_1$	E	A + B	$\{^2E,^1E\}^*$
T_1	T	A_2 + E	A_2 + E	A + $\{^2E,^1E\}^*$	A + $\{^2E,^1E\}^*$
T_2	T	B_2 + E	A_1 + E	B + $\{^2E,^1E\}^*$	A + $\{^2E,^1E\}^*$

$m_1 = 0.01$, $g_1 = 0.5$, and $g_2 = 0.5$ to obtain the dispersion relation and Chern number $\mathcal{C}$. As shown in Figs. S1(b) and S1(e) in the SM [38], the twofold crossing bands have Chern number $\mathcal{C}$ of ± 2, confirming that the spin-1 Weyl point splits into a quadratic Weyl node.

Similarly, we break the $\mathcal{C}_4$ symmetry by excluding $\mathcal{C}_{4z}$ operator from the generating elements in Eq. (2). The subduced representations ensure that the perturbation Hamiltonian V' shares the same basis functions with H_o. The perturbation Hamiltonian V' can be presented as

$$V' = \begin{pmatrix} 0 & h_1^* & h_2 \\ h_1 & 0 & h_3^* \\ h_2^* & h_3 & 0 \end{pmatrix},$$
$$h_1 = f - i(f_1 k_x - f_2 k_y + f_3 k_z), \quad (7)$$
$$h_2 = f - i(f_1 k_z - f_2 k_x + f_3 k_y),$$
$$h_3 = f - i(f_1 k_y - f_2 k_z + f_3 k_x),$$

where the coefficients f, f_1, f_2, and f_3 are nonzero real constants. Similarly, the Hamiltonian $H' = H_o + V'$ can describe the process that the spin-1 Weyl points evolve into quadratic Weyl nodes driven by $\mathcal{C}_4$ symmetry breaking. As shown in Figs. S1(c) and S1(f) in the SM [38], the twofold crossing bands have Chern number $\mathcal{C} = \pm 2$, showing that the spin-1 Weyl point transforms into the quadratic Weyl node by $\mathcal{C}_4$ symmetry breaking. Here, the parameters are chosen as $f = 0.1$, $f_1 = 0.2$, $f_2 = 0.3$, and $f_3 = 0.4$.

For the chiral space group, whose little group at Γ is isomorphic to the $O(432)$ group, the threefold spin-1 Weyl nodes emerging at Γ can be described by the above Hamiltonian in Eq. (4). As the $O(432)$ group is the supergroup of $T(32)$, the above analysis can be applied to $T(23)$, which also hosts spin-1 Weyl points at Γ. Using effective models and perturbation Hamiltonian, we have confirmed that the spin-1 Weyl node can evolve into the quadratic Weyl point if any perturbation drives the 3D IRs into 2D IRs. Besides, based on the above criteria and effective Hamiltonians, the space groups which host spin-1 Weyl points or quadratic Weyl nodes at Γ are summarized in the SM [38].

III. COMPUTATIONAL METHODS

We further employ first-principles calculations to confirm the transition behaviors discussed above. The first-principles calculations are performed based on the density functional theory (DFT) [41,42] using the Vienna *ab initio* simulation package (VASP) [43,44]. The core-valence interactions are treated by the projector augmented wave method [45]. The generalized gradient approximation (GGA) described by Perdew-Burke-Ernzerbof (PBE) function is used to describe the exchange-correlation functional [46,47]. The cutoff energy for plane waves is set to 500 eV. The phonon spectrum is calculated through the density functional perturbation theory (DFPT) approach [48] interfaced with the PHONOPY code [49]. A $3 \times 3 \times 3$ supercell is utilized to generate force matrix and the nonanalytical term is included to correct the dispersions near Γ. The comparison with and without the nonanalytical term correction is shown in Fig. S3. The surface states and Chern numbers $\mathcal{C}$ of $Rb_2Be_2O_3$ are calculated using the Green's function method based on the WANNIERTOOLS package [50,51].

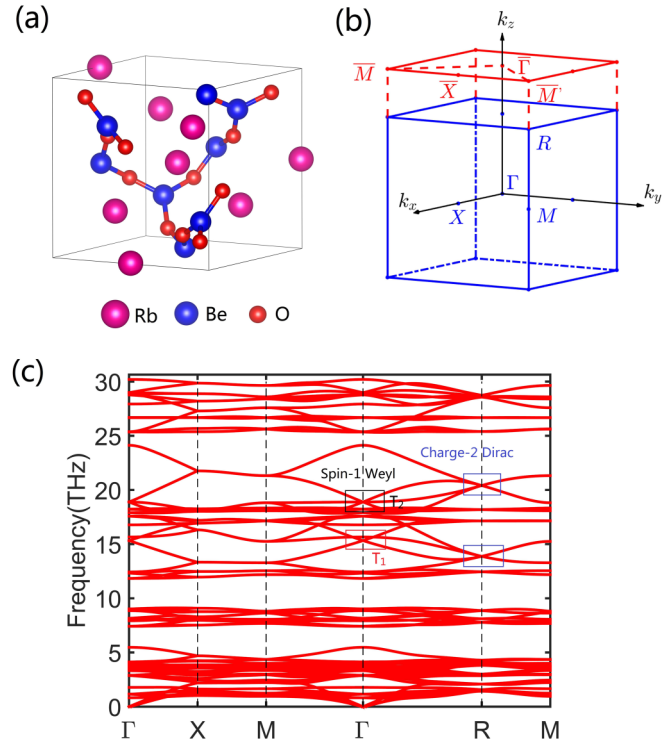

FIG. 2. (a) Crystalline structure of $Rb_2Be_2O_3$ with space group $P4_332$. Rb, Be, and O atoms are represented by pink, blue, and red spheres, respectively. (b) Bulk BZ and the (001) surface BZ. (c) Phonon spectrum along the high symmetry lines.

IV. MATERIALS REALIZATION

Here, we mainly focus on the cubic $Rb_2Be_2O_3$ and the other candidate $SrSi_2$ is provided in the SM [38]. As shown in Fig. 2(a), each unit cell contains eight Rb, eight Be, and 12 O atoms. Rb, Be, and O atoms occupy Wyckoff positions 8c (0.753, 0.253, 0.246), 8c (0.780, 0.219, 0.719), and 12d (0.625, 0.864, 0.386), respectively. The $Rb_2Be_2O_3$ is an insulator and the optimized lattice constant is 7.51 Å, which is in agreement with the previous work [52].

The group elements contain fourfold screw rotational symmetry $\widetilde{\mathcal{C}}_{4z} = \{\mathcal{C}_{4z}|\frac{3}{4}\frac{1}{4}\frac{3}{4}\}$ along the [001] axis, threefold rotational symmetry $\mathcal{C}_{3[111]}$ along the [111] direction, twofold screw rotational symmetries $\widetilde{\mathcal{C}}_{2x} = \{\mathcal{C}_{2x}|\frac{1}{2}\frac{1}{2}0\}$, $\widetilde{\mathcal{C}}_{2y} = \{\mathcal{C}_{2y}|0\frac{1}{2}\frac{1}{2}\}$, $\widetilde{\mathcal{C}}_{2z} = \{\mathcal{C}_{2z}|\frac{1}{2}0\frac{1}{2}\}$, and twofold rotational symmetries $\mathcal{C}_{2[011]}$, $\mathcal{C}_{2[101]}$, and $\mathcal{C}_{2[110]}$ along the [011], [101], and [110] axes, respectively. We plot the bulk BZ and projected surface BZ along the [001] direction, as well as the high symmetry points in Fig. 2(b). The phonon spectrum along the high symmetry lines is shown in Fig. 2(c). As expected, the threefold degenerate bands with 3D IRs at Γ form the spin-1 Weyl node [i.e., the T_2 modes marked by the black box in Fig. 2(c)], which is consistent with the above analysis. The enlarged drawing is shown in the upper panel of Fig. 3(a). It is worth noting that the T_2 modes near Γ are infrared silent

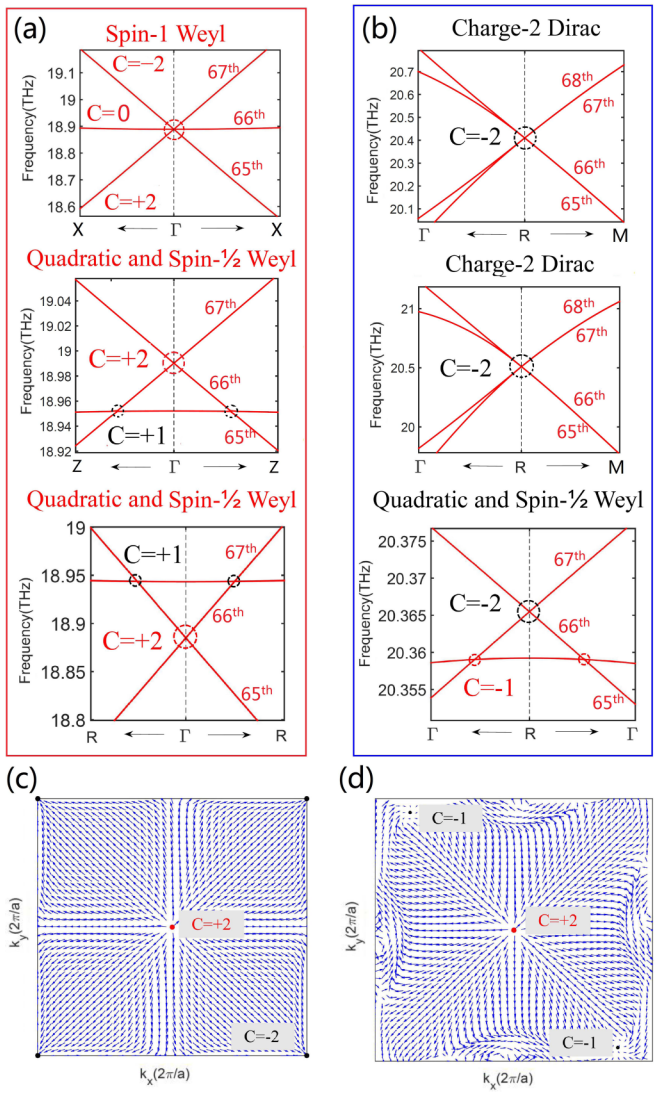

FIG. 3. The evolution of phonon spectra near the Γ and R points under symmetry variation. Each band is labeled by ordinal number. (a) The upper panel shows the enlarged phonon dispersion of $Rb_2Be_2O_3$ at Γ without external strain. The middle and bottom panels show the phonon spectra with $\mathcal{C}_3$ and $\mathcal{C}_4$ symmetry breaking, respectively. Z point located at the $\mathcal{C}_4$ axis when the strain is applied along the [001] direction. (b) The phonon dispersion near R is shown in the upper panel. The middle and bottom panels give the band spectra with $\mathcal{C}_3$ and $\mathcal{C}_4$ symmetry breaking, respectively. $\mathcal{C}$ labels bands in the top panel of (a), while $\mathcal{C}$ labels nodes in the other panels of (a) and (b). The Berry curvature distribution in the k_x-k_y plane with $\mathcal{C}_3$ (c) or $\mathcal{C}_4$ (d) symmetry breaking.

and robust against the nonanalytical correction, while the T_1 modes marked by the red box in Fig. 2(c) are infrared active and split [53]. The enlarged drawings are shown in Fig. S3. At the R point, there exist fourfold degenerate states which turn out to be charge-2 Dirac points [see the blue box in Fig. 2(c)] and the enlarged drawing is shown in the upper panel of Fig. 3(b). The three screw axes $\widetilde{\mathcal{C}}_{2x,2y,2z}$, satisfying the relation of $\{\widetilde{\mathcal{C}}_{2i}, \widetilde{\mathcal{C}}_{2j}\}=-2\delta_{ij}$ $(i, j = x, y, z)$, can give rise to a twofold degeneracy. In addition, the $\mathcal{C}_{2[110]}$ axis does not commute with the twofold screw rotational symmetry, leading to the fourfold charge-2 Dirac points (see more details in the SM [38]). To further examine the existence of the charge-2 Dirac point at R, we present the generating operators in the basis of $|u_{\mathbf{k}}\rangle$, $\widetilde{\mathcal{C}}_{2y}|u_{\mathbf{k}}\rangle$, $\mathcal{C}_{2[110]}|u_{\mathbf{k}}\rangle$, and $\widetilde{\mathcal{C}}_{2x}\mathcal{C}_{2[110]}|u_{\mathbf{k}}\rangle$ as below to construct the $\boldsymbol{k}\cdot\boldsymbol{p}$ model, where $|u_{\mathbf{k}}\rangle$ is the eigenstate of $\widetilde{\mathcal{C}}_{2z}$ with the eigenvalue $-i$ (see more details in the SM [38]),

$$\mathcal{C}_{3[111]}=\frac{\sqrt{2}}{2}\begin{pmatrix} e^{-i\frac{\pi}{12}} & e^{-i\frac{7\pi}{12}} & 0 & 0 \\ e^{i\frac{11\pi}{12}} & e^{-i\frac{7\pi}{12}} & 0 & 0 \\ 0 & 0 & e^{i\frac{\pi}{12}} & e^{i\frac{\pi}{12}} \\ 0 & 0 & e^{-i\frac{5\pi}{12}} & e^{i\frac{7\pi}{12}} \end{pmatrix},$$

$$\widetilde{\mathcal{C}}_{4z}=\begin{pmatrix} 0 & 0 & 0 & 1 \\ 0 & 0 & -1 & 0 \\ 0 & -i & 0 & 0 \\ -i & 0 & 0 & 0 \end{pmatrix},\ \mathcal{T}=\begin{pmatrix} 0 & 0 & -i & 0 \\ 0 & 0 & 0 & 1 \\ -i & 0 & 0 & 0 \\ 0 & 1 & 0 & 0 \end{pmatrix}\mathcal{K}, \tag{8}$$

where $\mathcal{K}$ is a complex conjugation operator. The transformation of momentum $\mathbf{k}$ under generating operators is listed below,

$$\begin{aligned} &(k_x, k_y, k_z) \xrightarrow{\mathcal{C}_{3[111]}} (k_z, k_x, k_y), \\ &(k_x, k_y, k_z) \xrightarrow{\widetilde{\mathcal{C}}_{4z}} (-k_y, k_x, k_z), \\ &(k_x, k_y, k_z) \xrightarrow{\mathcal{T}} (-k_x, -k_x, -k_z). \end{aligned} \tag{9}$$

Then a low-energy Hamiltonian is obtained as

$$H_1 = d\begin{pmatrix} k_z & -k_x - ik_y & 0 & 0 \\ -k_x + ik_y & -k_z & 0 & 0 \\ 0 & 0 & -k_z & -ik_x - k_y \\ 0 & 0 & ik_x - k_y & k_z \end{pmatrix}, \tag{10}$$

$$H_2 = U^{\dagger}H_1U = d\begin{pmatrix} \mathbf{k}\cdot\boldsymbol{\sigma} & 0 \\ 0 & \mathbf{k}\cdot\boldsymbol{\sigma} \end{pmatrix}, \tag{11}$$

where d is a nonzero constant and U is a unitary matrix. It is exactly the charge-2 Dirac point formed by two Weyl equations with the same chirality. For the spin-1 Weyl phonons, the Chern numbers $\mathcal{C}$ are defined on the threefold node for each degenerate band [see Fig. 3(a)]. To respect the no-go theorem, the spin-1 Weyl point with the Chern number $\mathcal{C} = +2$ (the sum of the Chern number $\mathcal{C}$ on the 65th and 66th bands) at Γ and the charge-2 Dirac node ($\mathcal{C} = -2$) at R come into pairs. However, between the 65th and 66th bands, there is only one spin-1 Weyl point with the Chern number $\mathcal{C} = +2$ (the Chern number of the 65th band) and the nodal walls emerge in the whole BZ. The no-go theorem is circumvented due to the existence of nodal walls [54]. The nodal walls can be understood by the combination operators $\widetilde{\mathcal{C}}_{2i}T$ $(i = x, y, z)$, which possess the product of $(\widetilde{\mathcal{C}}_{2i}T)^2 = -1$ and leave the $k_i = \pi$ $(i = x, y, z)$ planes invariant, giving rise to the twofold nodal walls at the boundary of BZ.

A. Symmetry breaking

We then evaluate the transition between spin-1 Weyl nodes and quadratic Weyl points by applying a strain with the pressure value of 0.98 GPa along the [001] direction, in which the $\mathcal{C}_3$ symmetry is broken. As shown in the middle panel of Fig. 3(a), the spin-1 Weyl node evolves into one quadratic Weyl node with $\mathcal{C} = +2$ (between the 66$^{\text{th}}$ and 67$^{\text{th}}$ bands) at Γ and one pair of spin-$\frac{1}{2}$ Weyl phonons with $\mathcal{C} = +1$ (between the 65$^{\text{th}}$ and 66$^{\text{th}}$ bands) lie along the C_4 axis. For the 65$^{\text{th}}$ and 66$^{\text{th}}$ bands, $\widetilde{\mathcal{C}}_{2i}\mathcal{T}$ $(i = x, y, z)$ can also protect the nodal walls at the boundary of BZ. Hence, there is only one pair of spin-$\frac{1}{2}$ Weyl phonons in the BZ to circumvent the no-go theorem. For the charge-2 Dirac node with $\mathcal{C} = -2$ at R, although the $\mathcal{C}_{2[110]}$ symmetry is broken, the relation $\{\widetilde{\mathcal{C}}_{2i}, \widetilde{\mathcal{C}}_{2j}\} = -2\delta_{ij}$ $(i, j = x, y, z)$ is conserved. The $\mathcal{T}$ symmetry maps the Weyl point into itself and preserves the chirality, still protecting the fourfold charge-2 Dirac points at R [see the middle panel of Fig. 3(b)].

We further apply another strain with the pressure value of 0.13 GPa along the [111] direction to break $\mathcal{C}_4$ symmetry. As expected, the spin-1 Weyl points at Γ are driven into one quadratic Weyl node with $\mathcal{C} = +2$ (between the 65$^{\text{th}}$ and 66$^{\text{th}}$ bands) and two spin-$\frac{1}{2}$ Weyl points with $\mathcal{C} = +1$ (between the 66$^{\text{th}}$ and 67$^{\text{th}}$ bands), as shown in the bottom panel of Fig. 3(a). In this case, the three bands derived from spin-1 Weyl nodes can be labeled by the eigenvalues $e^{\pm i\frac{2\pi}{3}}$ and 1 of $\mathcal{C}_3$ symmetry. The two bands with the eigenvalues $e^{\pm i\frac{2\pi}{3}}$ related by $\mathcal{T}$ symmetry can give rise to the quadratic Weyl point. Meanwhile, such two bands are allowed to intersect with the remaining single band with the eigenvalue of 1, forming two spin-$\frac{1}{2}$ Weyl nodes located along the $\mathcal{C}_3$ rotation axis.

At the R point, the charge-2 Dirac nodes are destroyed because the anticommutative relations among rotational screw axes $\widetilde{\mathcal{C}}_{2i}$ $(i = x, y, z)$ are broken. As the R point shares the same little group with Γ, it forms one quadratic Weyl node with $\mathcal{C} = -2$ (between the 66$^{\text{th}}$ and 67$^{\text{th}}$ bands) and two spin-$\frac{1}{2}$ Weyl points with $\mathcal{C} = -1$ (between the 65$^{\text{th}}$ and 66$^{\text{th}}$ bands), as shown in the bottom panel of Fig. 3(b). The 68$^{\text{th}}$ band near the R point does not appear in the current scale in the bottom panel of Fig. 3(b). To show the 68th band clearly, Fig. S5 is provided in the SM [38]. We then construct a perturbation Hamiltonian by excluding the operator $\widetilde{\mathcal{C}}_{4z}$ in Eq. (8) to elucidate such evolutionary process. The remaining $\widetilde{\mathcal{C}}_{3[111]}$ and $\mathcal{T}$ are the subduced representation with $\mathcal{C}_4$ symmetry breaking, which can ensure the obtained perturbation Hamiltonian V_1 sharing the same basis functions with H_1,

$$V_1 = \begin{pmatrix} 0 & V_1'^{\dagger} \\ V_1' & 0 \end{pmatrix}, \tag{12}$$

$$V_1' = \begin{pmatrix} (1-i)c_1 & c_1(1-\sqrt{3}) + c_2 i\widetilde{k} \\ c_1(1-\sqrt{3})i + c_2\widetilde{k} & c_1[\sqrt{3}-2+(2-\sqrt{3})i] \end{pmatrix},$$

$$\widetilde{k} = (\sqrt{3}-i)k_x + 2ik_y - (\sqrt{3}+i)k_z, \tag{13}$$

where the coefficients c_1 and c_2 are nonzero real constants (see more details in the SM [38]). As the perturbation Hamiltonian V_1 shares the same basis functions with Hamiltonian H_1, the charge-2 Dirac point at R with $\mathcal{C}_4$ symmetry breaking can be described by

$$H_1' = H_1 + V_1. \tag{14}$$

The band dispersion and Chern number $\mathcal{C}$ obtained by Eq. (14) are shown in Fig. S2, confirming that the charge-2 Dirac point exactly evolves into the quadratic Weyl node. Here, the parameters are chosen as $d = 1$, $c_1 = 0.03$, and $c_2 = 1$, respectively.

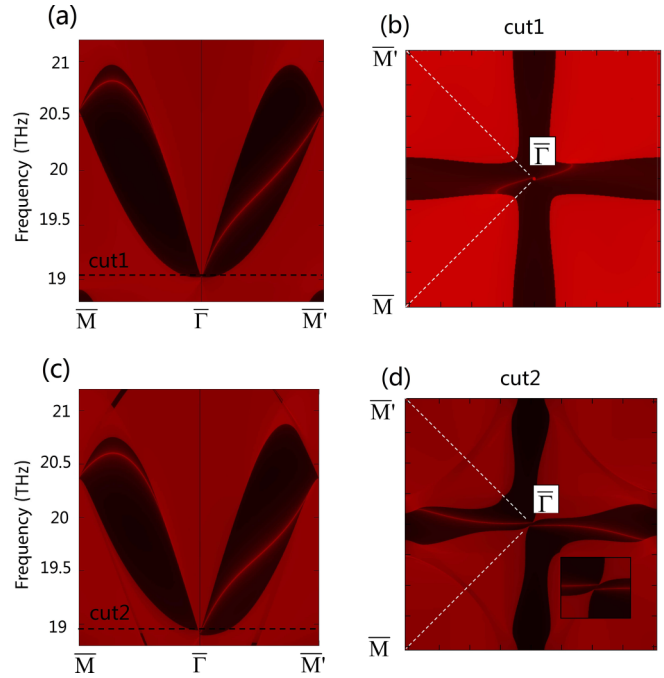

FIG. 4. (a) Projected LDOS on the (001) surface with $\mathcal{C}_3$ symmetry breaking, and (b) the corresponding isofrequency arcs at the frequency cut1 ($\omega = 19.045$ THz). (c) Projected LDOS on the (001) surface with $\mathcal{C}_4$ symmetry breaking, and (d) the corresponding isofrequency arcs at the frequency cut2 ($\omega = 18.943$ THz).

B. Berry curvature and edge states

We next examine the distribution of Berry curvature in the k_x-k_y plane when the C_3 symmetry is broken. As shown in Fig. 3(c), the quadratic Weyl node ($\mathcal{C} = +2$) at Γ and the charge-2 Dirac points ($\mathcal{C} = -2$) located at the corner of BZ act as the source and the drain of Berry curvature, respectively, reflecting these two different double Weyl phonons come in pairs. For the C_4 symmetry breaking, as shown in Fig. 3(d), the Berry curvature at Γ ($\mathcal{C} = +2$) flows into two spin-$\frac{1}{2}$ Weyl nodes ($\mathcal{C} = -1$), respectively, resulting in a triangular Weyl complex. It is worth pointing out that by breaking symmetry the spin-1 Weyl nodes exhibit diverse topological phases, such as quadratic Weyl, spin-$\frac{1}{2}$ Weyl, or triangular Weyl complex.

Finally, to illustrate the evolution of surface states when the crystal symmetries are broken, we calculate the surface local density of states (LDOS) and projected isofrequency surfaces. A semi-infinite surface is constructed to project LDOS on the (001) surface. The quadratic Weyl node at the Γ point is projected to $\overline{\Gamma}$, and the charge-2 Dirac point located at R is projected to $\overline{M}$. The obtained LDOS along the high symmetry lines on the (001) surface is plotted in Fig. 4(a), and the corresponding isofrequency contour at $\omega = 19.045$ THz is

shown in Fig. 4(b). To respect the Chern number, there are two visible surface states that come out from the projection of quadratic Weyl node and are terminated at the charge-2 Dirac point, which is coincident with the Berry curvature distribution. When the uniaxial strain is applied along the [111] direction, the surface states that start at the quadratic Weyl point ($\mathcal{C} = +2$) at $\overline{\Gamma}$ are obscured in bulk bands, whereas two arcs originated from the two spin-$\frac{1}{2}$ Weyl nodes ($\mathcal{C} = +1$) are clearly visible as shown in Fig. 4(c). The isofrequency surface at $\omega = 18.943$ is shown in Fig. 4(d), and there are two arcs that exactly come out from two spin-$\frac{1}{2}$ Weyl nodes and are terminated at the quadratic Weyl point near the $\overline{M}$ point.

V. SUMMARY

In summary, through a systematic analysis of the IRs of chiral point groups, we present that the spin-1 Weyl nodes governed by 3D IRs of $O(432)$ or $T(23)$ groups can evolve into quadratic Weyl points if the energy level degenerations follow $T = A \oplus E$. We show the splitting mechanism by symmetry arguments and the low-energy $\boldsymbol{k} \cdot \boldsymbol{p}$ Hamiltonian. Based on our recipe, all the space groups hosting spin-1 or quadratic Weyl phonons at Γ are figured out. Furthermore, $Rb_2Be_2O_3$ is an ideal candidate to show the evolutionary process of corresponding Berry curvature and surface states. The long surface arcs spanning the whole BZ are easily measured in experiments, which also provide a promising unidirectional phonon propagation channel. Our findings offer further insights into double Weyl phonons and provide an experimental platform to investigate the splitting behavior of double Weyl bosons, as well as the possibility to fabricate pressure-controlled topological thermal devices.

ACKNOWLEDGMENTS

This work is supported by the Guangdong Natural Science Funds for Distinguished Young Scholars (Grant No. 2017B030306008), National Natural Science Foundation of China (NSFC) Grant No. 11974160, the Science, Technology and Innovation Commission of Shenzhen Municipality (Grant No. ZDSYS20190902092905285), the Guangdong Provincial Key Laboratory of Computational Science and Material Design (Grant No. 2019B030301001), and the Center for Computational Science and Engineering at Southern University of Science and Technology.

[1] M. Z. Hasan and C. L. Kane, Rev. Mod. Phys. **82**, 3045 (2010).
[2] X.-L. Qi and S.-C. Zhang, Rev. Mod. Phys. **83**, 1057 (2011).
[3] N. P. Armitage, E. J. Mele, and A. Vishwanath, Rev. Mod. Phys. **90**, 015001 (2018).
[4] C. L. Kane and E. J. Mele, Phys. Rev. Lett. **95**, 146802 (2005).
[5] B. A. Bernevig, T. L. Hughes, and S.-C. Zhang, Science **314**, 1757 (2006).
[6] Z. Wang, Y. Sun, X.-Q. Chen, C. Franchini, G. Xu, H. Weng, X. Dai, and Z. Fang, Phys. Rev. B **85**, 195320 (2012).
[7] Z. Liu, B. Zhou, Y. Zhang, Z. Wang, H. Weng, D. Prabhakaran, S.-K. Mo, Z. Shen, Z. Fang, X. Dai *et al.*, Science **343**, 864 (2014).
[8] A. C. Potter, I. Kimchi, and A. Vishwanath, Nat. Commun. **5**, 5161 (2014).
[9] P. J. Moll, N. L. Nair, T. Helm, A. C. Potter, I. Kimchi, A. Vishwanath, and J. G. Analytis, Nature (London) **535**, 266 (2016).
[10] X. Wan, A. M. Turner, A. Vishwanath, and S. Y. Savrasov, Phys. Rev. B **83**, 205101 (2011).
[11] H. Weng, C. Fang, Z. Fang, B. A. Bernevig, and X. Dai, Phys. Rev. X **5**, 011029 (2015).
[12] S.-Y. Xu, I. Belopolski, N. Alidoust, M. Neupane, G. Bian, C. Zhang, R. Sankar, G. Chang, Z. Yuan, C.-C. Lee *et al.*, Science **349**, 613 (2015).
[13] A. A. Burkov, M. D. Hook, and L. Balents, Phys. Rev. B **84**, 235126 (2011).
[14] Y. J. Jin, Z. J. Chen, B. W. Xia, Y. J. Zhao, R. Wang, and H. Xu, Phys. Rev. B **98**, 220103(R) (2018).
[15] Y. Jin, R. Wang, and H. Xu, Nano lett. **18**, 7755 (2018).
[16] B. W. Xia, R. Wang, Z. J. Chen, Y. J. Zhao, and H. Xu, Phys. Rev. Lett. **123**, 065501 (2019).
[17] Q.-B. Liu, Y. Qian, H.-H. Fu, and Z. Wang, npj Comput. Mater. **6**, 95 (2020).
[18] T. Zhang, R. Takahashi, C. Fang, and S. Murakami, Phys. Rev. B **102**, 125148 (2020).
[19] J. Li, Q. Xie, J. Liu, R. Li, M. Liu, L. Wang, D. Li, Y. Li, and X.-Q. Chen, Phys. Rev. B **101**, 024301 (2020).
[20] Q. Xie, J. Li, S. Ullah, R. Li, L. Wang, D. Li, Y. Li, S. Yunoki, and X.-Q. Chen, Phys. Rev. B **99**, 174306 (2019).
[21] X. Huang, L. Zhao, Y. Long, P. Wang, D. Chen, Z. Yang, H. Liang, M. Xue, H. Weng, Z. Fang *et al.*, Phys. Rev. X **5**, 031023 (2015).
[22] D. T. Son and B. Z. Spivak, Phys. Rev. B **88**, 104412 (2013).
[23] A. A. Zyuzin and A. A. Burkov, Phys. Rev. B **86**, 115133 (2012).
[24] H. Jia, R. Zhang, W. Gao, Q. Guo, B. Yang, J. Hu, Y. Bi, Y. Xiang, C. Liu, and S. Zhang, Science **363**, 148 (2019).
[25] B. Bradlyn, J. Cano, Z. Wang, M. Vergniory, C. Felser, R. J. Cava, and B. A. Bernevig, Science **353**, aaf5037 (2016).
[26] J. L. Manes, Phys. Rev. B **85**, 155118 (2012).
[27] C. Fang, M. J. Gilbert, X. Dai, and B. A. Bernevig, Phys. Rev. Lett. **108**, 266802 (2012).
[28] G. Xu, H. Weng, Z. Wang, X. Dai, and Z. Fang, Phys. Rev. Lett. **107**, 186806 (2011).
[29] S.-M. Huang, S.-Y. Xu, I. Belopolski, C.-C. Lee, G. Chang, T.-R. Chang, B. Wang, N. Alidoust, G. Bian, M. Neupane *et al.*, Proc. Natl. Acad. Sci. USA **113**, 1180 (2016).
[30] T. Zhang, Z. Song, A. Alexandradinata, H. Weng, C. Fang, L. Lu, and Z. Fang, Phys. Rev. Lett. **120**, 016401 (2018).
[31] H. Miao, T. T. Zhang, L. Wang, D. Meyers, A. H. Said, Y. L. Wang, Y. G. Shi, H. M. Weng, Z. Fang, and M. P. M. Dean, Phys. Rev. Lett. **121**, 035302 (2018).
[32] R. Wang, B. W. Xia, Z. J. Chen, B. B. Zheng, Y. J. Zhao, and H. Xu, Phys. Rev. Lett. **124**, 105303 (2020).
[33] Z. Huang, Z. Chen, B. Zheng, and H. Xu, npj Comput. Mater. **6**, 87 (2020).

[34] P. Tang, Q. Zhou, and S.-C. Zhang, Phys. Rev. Lett. **119**, 206402 (2017).
[35] G. Chang, S.-Y. Xu, B. J. Wieder, D. S. Sanchez, S.-M. Huang, I. Belopolski, T.-R. Chang, S. Zhang, A. Bansil, H. Lin *et al.*, Phys. Rev. Lett. **119**, 206401 (2017).
[36] S.-K. Jian and H. Yao, Phys. Rev. B **92**, 045121 (2015).
[37] S.-K. Jian and H. Yao, Phys. Rev. B **96**, 155112 (2017).
[38] See Supplemental Material at http://link.aps.org/supplemental/10.1103/PhysRevB.103.104101 for the evolution of the Wilson loop based on the low-energy effective models in the main text. The four eigenstates related to charge-2 Dirac point and the involved space groups hosting spin-1 or quadratic Weyl phonons are also provided.
[39] C. Bradley and A. Cracknell, *The Mathematical Theory of Symmetry in Solids: Representation Theory for Point Groups and Space Groups* (Clarendon Press, Oxford, 1972).
[40] H. Weng, R. Yu, X. Hu, X. Dai, and Z. Fang, Adv. Phys. **64**, 227 (2015).
[41] P. Hohenberg and W. Kohn, Phys. Rev. **136**, B864 (1964).
[42] W. Kohn and L. J. Sham, Phys. Rev. **140**, A1133 (1965).
[43] G. Kresse and J. Furthmüller, Phys. Rev. B **54**, 11169 (1996).
[44] G. Kresse and J. Furthmïller, Comput. Mater. Sci. **6**, 15 (1996).
[45] P. E. Blöchl, Phys. Rev. B **50**, 17953 (1994).
[46] J. P. Perdew, K. Burke, and M. Ernzerhof, Phys. Rev. Lett. **77**, 3865 (1996).
[47] J. P. Perdew, K. Burke, and M. Ernzerhof, Phys. Rev. Lett. **78**, 1396(E) (1997).
[48] X. Gonze and C. Lee, Phys. Rev. B **55**, 10355 (1997).
[49] A. Togo, F. Oba, and I. Tanaka, Phys. Rev. B **78**, 134106 (2008).
[50] M. L. Sancho, J. L. Sancho, and J. Rubio, J. Phys. F: Met. Phys. **14**, 1205 (1984).
[51] Q. Wu, S. Zhang, H.-F. Song, M. Troyer, and A. A. Soluyanov, Comput. Phys. Commun. **224**, 405 (2018).
[52] S. P. Ong, S. Cholia, A. Jain, M. Brafman, D. Gunter, G. Ceder, and K. A. Persson, Comput. Mater. Sci. **97**, 209 (2015).
[53] V. Caciuc, A. V. Postnikov, and G. Borstel, Phys. Rev. B **61**, 8806 (2000).
[54] Z.-M. Yu, W. Wu, Y. X. Zhao, and S. A. Yang, Phys. Rev. B **100**, 041118(R) (2019).